

Anomalous photovoltaics in Janus MoSSe monolayers

Received: 21 May 2024

Accepted: 18 December 2024

Published online: 09 January 2025

 Check for updates

Chang Liu^{1,9}, Tianyu Liang^{2,9}, Xin Sui^{1,9}, Lena Du^{3,9}, Quanlin Guo², Guodong Xue², Chen Huang², Yilong You², Guangjie Yao², Mengze Zhao², Jianbo Yin⁴, Zhipei Sun⁵, Hao Hong^{2,6} ✉, Enge Wang^{1,7,8} ✉ & Kaihui Liu^{1,2,8} ✉

The anomalous photovoltaic effect (APE) in polar crystals is a promising avenue for overcoming the energy conversion efficiency limits of conventional photoelectric devices utilizing p-n junction architectures. To facilitate effective photocarrier separation and enhance the APE, polar materials need to be thinned down to maximize the depolarization field. Here, we demonstrate Janus MoSSe monolayers (~0.67 nm thick) with strong spontaneous photocurrent generation. A photoresponsivity up to 3 mA/W, with ~1% external quantum efficiency and ultrafast photoresponse (~50 ps) were observed in the MoSSe device. Moreover, unlike conventional 2D materials that require careful twist alignment, the photovoltage can be further scaled up by simply stacking the MoSSe layers without the need for specific control on interlayer twist angles. Our work paves the way for the development of high-performance, flexible, and compact photovoltaics and optoelectronics with atomically engineered Janus polar materials.

The anomalous photovoltaic effect (APE) emerges when photoexcited electron-hole pairs undergo separation driven by spontaneous polarization within asymmetric single-phase materials^{1,2}. APE avoids the built-in electric field established by a p-n junction and thus is highly desirable for achieving high photovoltaic conversion efficiency to surpass the Shockley–Queisser limit^{3–6}. To induce pronounced APE, manipulating the symmetry and dimensions of the material is crucial for strengthening the polarization and enhancing the light-matter interaction^{7–10}. In conventional three-dimensional bulk materials, intrinsic point group symmetries are strictly dictated by the lattice arrangement. APE can be caused by the microscopic grains or ferroelectric domain walls, requiring a controllable granular interface or distorted structure^{11–14}.

Two-dimensional (2D) van der Waals (vdW) materials with reduced dimensionality intrinsically have an atomically-thin thickness and provide the opportunity to artificially design symmetries at the interfaces or surfaces^{15–31}. For instance, by precisely aligning bilayer transition metal dichalcogenides (TMDs) with a twist angle of exactly zero, out-of-plane electric polarization occurs at the interface^{25,26}. Heterostructures composed of atomic-layered WS₂ and black phosphorus, with rationally designed stacking, exhibit interfacial in-plane polarization²⁰. These emerging polarizations produce a prominent APE with high quantum efficiency for energy conversion. Nevertheless, this symmetry breaking is extrinsically localized to the interface between the layers, necessitating the incorporation of a multilayered structure and meticulous control over the interlayer stacking order.

¹International Centre for Quantum Materials, Collaborative Innovation Centre of Quantum Matter, Peking University, Beijing, China. ²State Key Lab for Mesoscopic Physics, Frontiers Science Centre for Nano-optoelectronics, School of Physics, Peking University, Beijing, China. ³Department of Physics, Capital Normal University, Beijing, China. ⁴State Key Laboratory of Advanced Optical Communications System and Networks, School of Electronics, Peking University, Beijing, China. ⁵QTF Centre of Excellence, Department of Electronics and Nanoengineering, Aalto University, Espoo, Finland. ⁶Interdisciplinary Institute of Light-Element Quantum Materials and Research Centre for Light-Element Advanced Materials, Peking University, Beijing, China. ⁷Tsientang Institute for Advanced Study, Beijing, Zhejiang, China. ⁸Songshan Lake Materials Laboratory, Dongguan, China. ⁹These authors contributed equally: Chang Liu, Tianyu Liang, Xin Sui, Lena Du. ✉e-mail: haohong@pku.edu.cn; egwang@pku.edu.cn; khliu@pku.edu.cn

Furthermore, the interlayer polarization and its associated photocurrent generation are susceptible to the internal local strain or external electric field^{27–29} due to the weak nature of the vdW interactions.

An alternative approach involves atomic manufacturing of the surfaces of the 2D materials for symmetry breaking in a unit material. By using precise composition engineering through selective atom replacement on one side of the 2D TMDs, a Janus monolayer structure with an asymmetric atomic lattice can be synthesized^{32–35}. The presence of spatially distinct atoms (for example, sulfur (S) and selenium (Se)) results in the breaking of the mirror symmetry and inversion symmetry, leading to pronounced intrinsic out-of-plane polarization³², a strong piezoelectric effect^{36,37} and high harmonic generation³⁸ in MoSSe. The substantial inherent polarity in this system should also produce an APE with efficient optoelectronic conversion, which still needs to be fully explored.

Here, we demonstrate Janus MoSSe-based devices for achieving APE with giant responsivity within the 2D material family. This superior responsivity benefits from the robust intrinsic polarization from its atomic substitutional structure, the enhanced depolarization field in thin thickness down to the monolayer, and the boosted light-matter interaction involving excitons. Notably, the photovoltage of each monolayer can be easily scaled, independent of the intricate interlayer twisting or sliding.

Results

Polar structure of the Janus MoSSe monolayer

In our experiment, a local element supply method was developed to synthesize a Janus MoSSe monolayer (see Methods for details) with an intrinsic out-of-plane polarization perpendicular to the film by

substituting the top sulfur (S) atoms with selenium (Se) atoms (Fig. 1a). Nondestructive optical Raman spectroscopy, photoluminescence (PL) spectroscopy, and X-ray photoelectron spectroscopy (XPS) were conducted to confirm the Janus MoSSe structure (Fig. 1b and Supplementary Fig. S1 and Fig. S2). Compared with the Raman signals of the MoS₂ monolayer (with A_{1g} at -406 cm^{-1} and E_{2g} at -386 cm^{-1}) and MoSe₂ monolayer (with A_{1g} at -243 cm^{-1} and E_{2g} at -289 cm^{-1}), MoSSe exhibits a shifted out-of-plane A_{1g} mode located at -290 cm^{-1} and an in-plane E_{2g} mode located at -356 cm^{-1} due to the broken out-of-plane symmetry and lattice constant variation. The representative PL peak of MoSSe falls between those of MoS₂ (at -1.84 eV) and MoSe₂ (at -1.52 eV), at -1.70 eV , as illustrated in Fig. 1c. To directly determine the atomic structure of MoSSe, high-angle annular dark-field scanning transmission electron microscopy (STEM) was used to image the cross-section of a MoSSe monolayer. Since the image contrast is proportional to the atomic number, the S and Se atoms located at the bottom and top of MoSSe could be clearly distinguished, respectively (Fig. 1d).

To further reveal the intrinsic polarization properties of the MoSSe sample, incident-angle dependent second-harmonic generation (SHG) measurement was conducted (schematically shown in the inset of Fig. 1e). The incident angle could be tuned accordingly by moving the beam position at the objective back aperture using a translation stage (Supplementary Fig. S3). The SHG intensity ratio (I_p/I_s) between the p and s polarizations of the MoSSe sample increases with increasing incident angle (Fig. 1e), which directly shows the contribution from the out-of-plane dipole of the MoSSe monolayer. By carefully analysing the angle-dependent SHG intensity ratio (Supplementary Note 1), the second-order susceptibility associated with the out-of-plane dipole can be roughly extracted, and $\chi_{xxx}^{(2)}$ is $\sim 0.08\chi_{xxx}^{(2)}$ at the 800 nm pump wavelength.

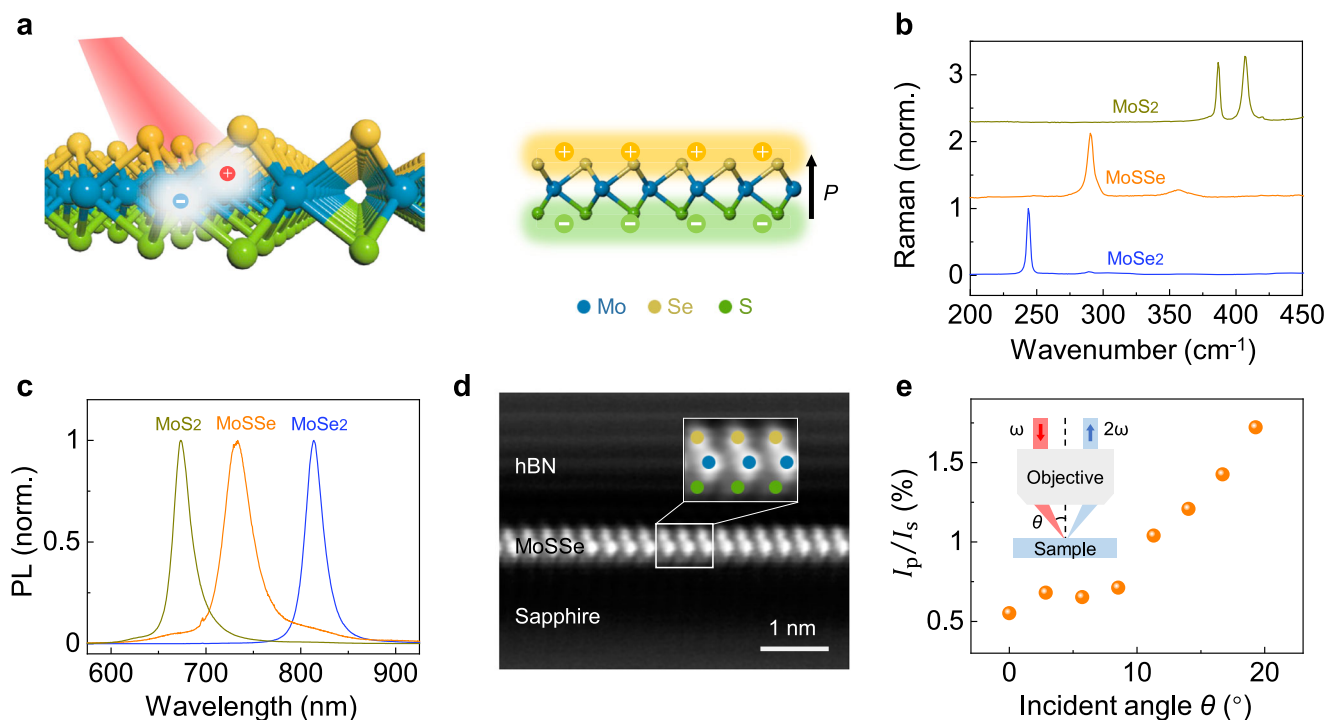


Fig. 1 | Polar structure of the Janus MoSSe monolayer. **a** Structure of the Janus MoSSe monolayer and the generation of the electron-hole pairs (circles with + and – signs) under optical illumination (left). The intrinsic polarization (P) existing in the MoSSe monolayer results in the spontaneous separation of electrons and holes (right). Typical Raman (**b**) and photoluminescence (PL) (**c**) spectra of MoS₂, MoSSe and MoSe₂ monolayers. **d** Scanning transmission electron microscopy (STEM) image of the cross-section of the MoSSe monolayer, showing the asymmetric

structure with Se (brown) on top and S (green) at the bottom. **e** Incident angle-dependent second-harmonic generation (SHG) intensity ratio (I_p/I_s) between the p and s polarizations in a MoSSe monolayer. The inset shows a schematic of the out-of-plane SHG measurement of the MoSSe sample. The incident angle θ can be tuned accordingly by moving the beam position at the objective back aperture using a translation stage. The incident light and SHG signal are denoted with ω and 2ω , respectively.

Spontaneous photovoltaic effect in the MoS₂ devices

The asymmetric atomic structure with out-of-plane polarization in the MoS₂ monolayer generates a giant spontaneous photovoltaic effect. MoS₂ (monolayer or few-layer)-based devices were fabricated by sandwiching graphene layers as electrodes. The entire devices were encapsulated by boron nitride (BN) films (Fig. 2a). An optical image of a typical MoS₂ bilayer device is shown in Fig. 2b. The effective area of the device is marked by the red solid line. Under dark conditions, the device shows a linear current-voltage (*I*-*V*) curve crossing the zero point. Upon optical illumination (with a wavelength of 633 nm), a giant spontaneous photocurrent is observed, and the *I*-*V* curve shifts away from the origin at zero bias voltage (orange line in Fig. 2d). A device with a similar structure was fabricated using a 2H (hexagonal) stacked MoS₂ bilayer for comparison. In contrast to that of the MoS₂ device, the measured short-circuit *I*-*V* curve of the MoS₂ device shows no spontaneous photocurrent at zero bias voltage (olive line in Fig. 2d). Notably, the symmetric *I*-*V* curves indicate a negligible p-n junction effect in our devices. By scanning the device with a focused laser spot, the measured short-circuit photocurrent mapping at zero bias voltage was found to be consistent with the effective sample area (Fig. 2b, c). The line scan results show that the spontaneous photovoltaic effect only occurs in the effective area of MoS₂ with both top and bottom graphene electrodes (Fig. 2e). This observation excludes the photocurrent origin from the thermal effect induced by the laser irradiation and the p-n junction between MoS₂ and graphene.

The prominent spontaneous photovoltaic effect can be scaled up with increasing MoS₂ layer number. In contrast to 3R (rhombohedral) MoS₂, which exhibits an interfacial spontaneous photovoltaic voltage under a strict stacking order, the intrinsic polarization in MoS₂

increases the open-circuit voltage with additional layers, irrespective of interlayer twisting or sliding. The out-of-plane polarization aligns in the same direction, and the stacking does not diminish the polarization of the crystal (Supplementary Fig. S4 and Fig. S5). Figure 2f shows the layer number-dependent open-circuit photovoltage and short-circuit photocurrent of three different devices with 1-3 layers of MoS₂, respectively (Supplementary Fig. S6, S7). Remarkably, in the MoS₂ monolayer device, a significant spontaneous photocurrent (-125 nA) is generated with an open-circuit photovoltage of approximately 0.3 mV. For the three-layer MoS₂ device, the photovoltage increases to nearly 0.9 mV and the photocurrent is almost unchanged.

Ultrafast response of spontaneous photocurrent in MoS₂ devices

In addition to the photoresponsivity, the photoresponse time is also a vital device parameter, because it determines the intrinsic bandwidth (*f*) of a photodetector. We used ultrafast time-resolved photocurrent autocorrelation spectroscopy to determine the photoresponse time^{39,40}. In our experiment, two successive laser pulses were applied to the MoS₂ device at the same point with a time delay (Δt), as shown in Fig. 3a. When two pulses overlap in time ($\Delta t = 0$), the photocurrent reaches its minimum value due to the saturation behavior at higher incident powers. When the time delay is apart from zero ($\Delta t < 0$ or $\Delta t > 0$), the photocurrent gradually increases. Specifically, the dip of the photocurrent curve reflects the detector's ability to distinguish two successive pulses. An exponential fit to the rising curve yields a typical response time of $\tau = -50$ ps (Fig. 3b, c), corresponding to an intrinsic bandwidth of $f = 0.55/\tau = 11$ GHz, which is independent of the pump power. Regarding the noise characteristics, the noise level of the

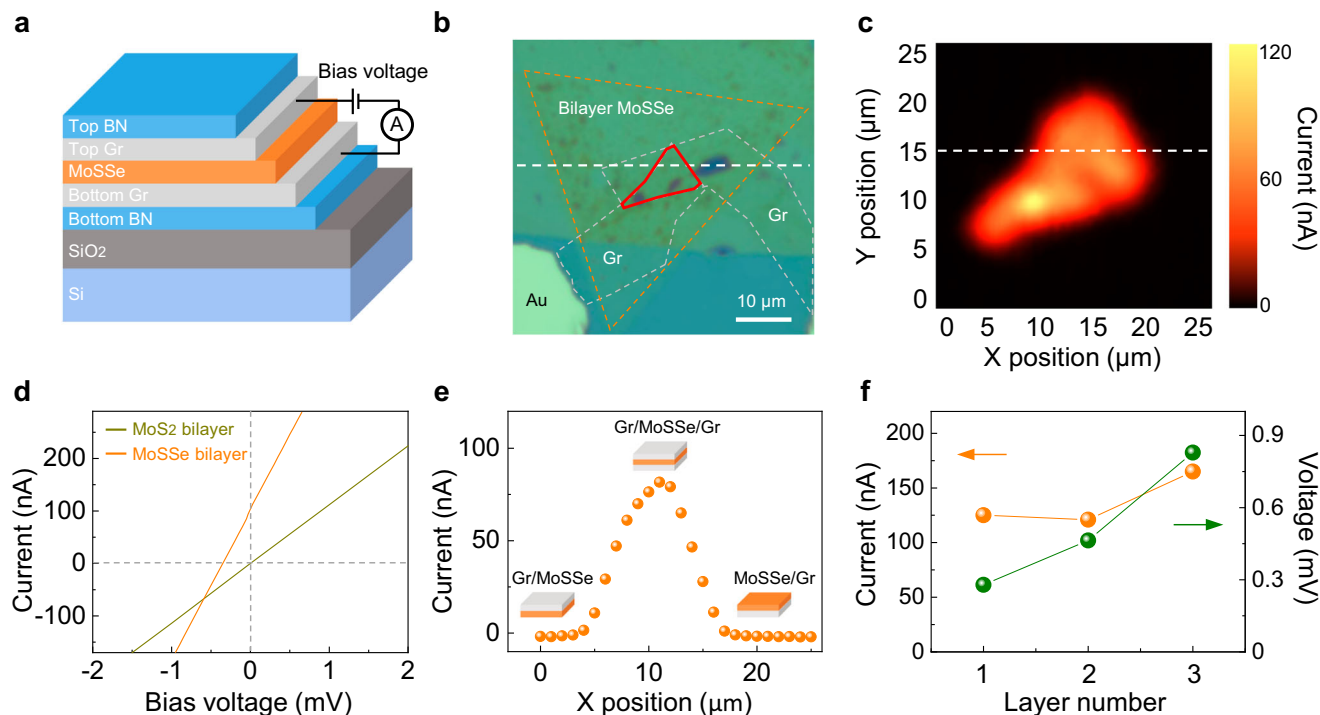


Fig. 2 | Spontaneous photovoltaic effect in the MoS₂ devices. **a** Schematic of the photovoltaic device. The heterostructure consists of a MoS₂ film sandwiched between two graphene electrodes, which is further encapsulated by BN films. **b** Optical image of the MoS₂ bilayer device. The effective area (overlap area of the MoS₂ bilayer, top and bottom graphene electrodes) is marked by the red solid line. The MoS₂ bilayer and graphene electrodes are outlined by orange and gray dashed lines, respectively. **c** Short-circuit photocurrent mapping result of the MoS₂ bilayer device, corresponding to the area marked by the red solid line in (b). **d** Short-circuit photocurrent of the MoS₂ bilayer and MoS₂ bilayer devices as a

function of bias voltage under the same illumination conditions. The nonzero photocurrent at zero bias voltage indicates spontaneous photovoltaic responses in the MoS₂ device. **e** Line scan photocurrent result of the MoS₂ device indicated by the horizontal white dashed line in (b) and (c). The different photocurrent results in and out of the effective area with different configurations help to demonstrate the origin of the spontaneous photocurrent. **f** Layer dependence of the short-circuit current and open-circuit voltage in the MoS₂ device. With increasing layer number, the photocurrent remains nearly unchanged, while the voltage increases accordingly.

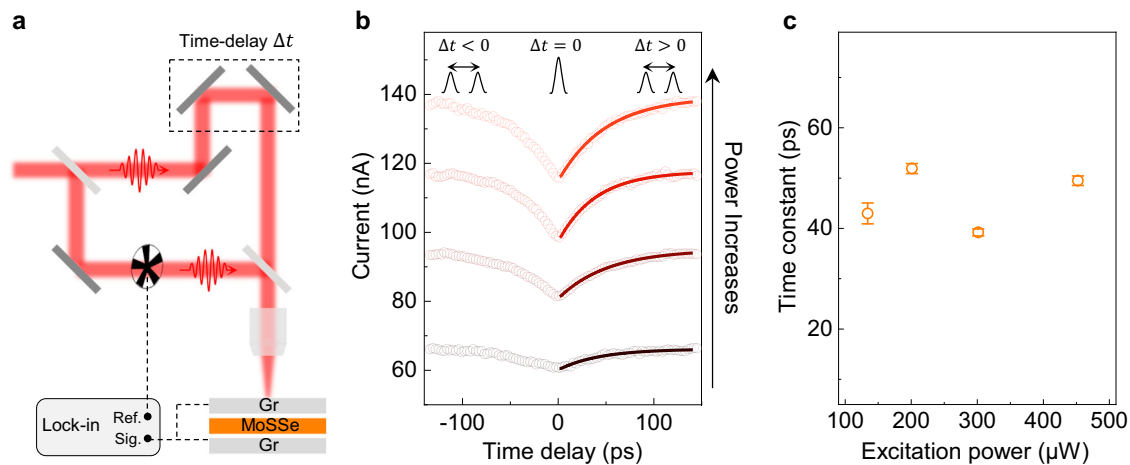


Fig. 3 | Ultrafast response of the spontaneous photovoltaic effect in the MoSSe devices. **a** Schematic of the ultrafast time-resolved photocurrent measurement. The two ultrafast pulses with a time delay Δt are focused collinearly on the device. The generated photocurrent is measured by a lock-in amplifier. **b** Autocorrelation photocurrent of the device as a function of the time delay between the two pulses at zero bias voltage, with increasing excitation power from bottom to the top. The

circles are the experimental data, and the solid lines are the exponential fits. The inset black curves at the top represent the pump and probe pulses, and the black arrow denotes the time delay. **c** Response time constant of the MoSSe-based device at different incident power, which is extracted from the exponential fitting of the photocurrent-delay curves in (b). Here, the error bars show the standard errors of the fitting parameters.

device was obtained to be $-10^{-21} \text{ A}^2 \text{ Hz}^{-1}$ with zero bias voltage at room temperature (Supplementary Fig. S8). This value is expected given that the device resistance is relatively small ($\sim 2 \text{ k}\Omega$). When operating at high frequency, the noise level can be substantially suppressed. Therefore, the MoSSe-based devices show the advantage at high frequency with the intrinsic ultrafast photoresponse.

Mechanism of photocurrent generation in MoSSe devices

In the followings, we discuss the origin of the giant spontaneous photovoltaic effect in the MoSSe devices. In an asymmetric polar structure, APE can be caused by three different spontaneous photovoltaic mechanisms. First, the shift current and injection current are second-order nonlinear optical effects governed by the quantum geometric properties and occurs in materials with broken inversion symmetry^{41,42}, which have notable features and can be distinguished from other mechanisms, including unique polarization and power dependence. Second, due to the residual uncompensated polarization charge at the polar material/electrode interface, the depolarization field can also drive the separation of the electron-hole pairs and lead to prominent APE, especially in the thin polar layer⁴³ (Fig. 4a).

In the MoSSe devices, the generated photocurrent is closely related to the optical absorption of the MoSSe film (Fig. 4b). The photocurrent responsivity spectrum shows two peaks at $\sim 700 \text{ nm}$ and $\sim 625 \text{ nm}$, which correspond to the absorption of the A and B excitons of MoSSe, respectively (Fig. 4b and Supplementary Fig. S2c). With further decreases in the excitation wavelength, the photoresponsivity reaches above 3 mA/W with a laser spot of approximately $1 \mu\text{m}^2$ at 450 nm . Regarding the power dependence of the photocurrent, the generated spontaneous current linearly increases with the incident laser power at a relatively low excitation power (Fig. 4c). Notably, the curve shows a clear deviation from linear behavior towards saturation at higher excitation power.

The spontaneous photocurrent in MoSSe devices is independent of the polarization of the incident light under normal incidence. By varying the orientation direction of the waveplates (θ_1 and θ_2 are the angles between the polarization direction of the incident light and the fast axis of the $\lambda/2$ and $\lambda/4$ waveplates, respectively), the polarization of the incident light upon the sample can be continuously modulated (Fig. 4d). As expected, the photocurrent remains nearly unchanged under different linear polarization directions (Fig. 4e) and different

ellipticities (Fig. 4f). While for the scheme of oblique incidence, the photocurrent evolves with the waveplate angle and reaches its maximum when the light polarization is totally in-plane, due to absorption anisotropy (Supplementary Fig. S9). Together with the power-dependent results, it's indicated that the photocurrent is not dominated by the shift current mechanism, but more like the depolarization field mechanism.

In the depolarization field-induced APE scenario, the intrinsic out-of-plane polarization (P) existing in MoSSe induces surface charges (σ) with opposite signs in the top and bottom graphene electrodes. The electrons in the electrodes can screen the surface charges, and two dipoles with the same direction form at the two electrode-sample interfaces. Each dipole is responsible for an electrostatic potential drop (ΔV) in the same direction (Fig. 4a and Supplementary Fig. S10). Since the induced charges cannot fully compensate for the polarization charges in MoSSe, the resulting depolarization field inside the material drives the separation of the electron-hole pairs, which can be collected by the graphene electrodes via interfacial charge transfer, thus forming a spontaneous photocurrent. In general, the depolarization field established is proportional to the induced potential difference and inversely proportional to the film thickness. Therefore, a thinner polar film will lead to a stronger depolarization field and more efficient APE. In our experiment, the magnitude of the depolarization field can be estimated by the band diagram and related open circuit voltage, which gives the upper bound value on the order of $\sim 10^4 \text{ kV/cm}$ (Supplementary Note 2).

Discussion

Compared with other photovoltaic materials, Janus MoSSe has numerous figures of merit. The polarization state of MoSSe originates from the intrinsic asymmetric atomic lattice that can stably exist at the thickness of $\sim 0.67 \text{ nm}$. It's expected to be the thinnest photovoltaic devices with giant photocurrent responsivity within the entire family of 2D material (Supplementary Table S1 and Table S2). Moreover, the enhanced depolarization field and the reduced diffusion length of photocarriers increase the efficiency. On the other hand, MoSSe-based devices are also limited by the typical disadvantages such as lack of polarization switching, existence of strain and extrinsic contamination, and the challenge of mass production. Overall, Janus TMDs are promising candidates to facilitate the development of miniaturized, high-

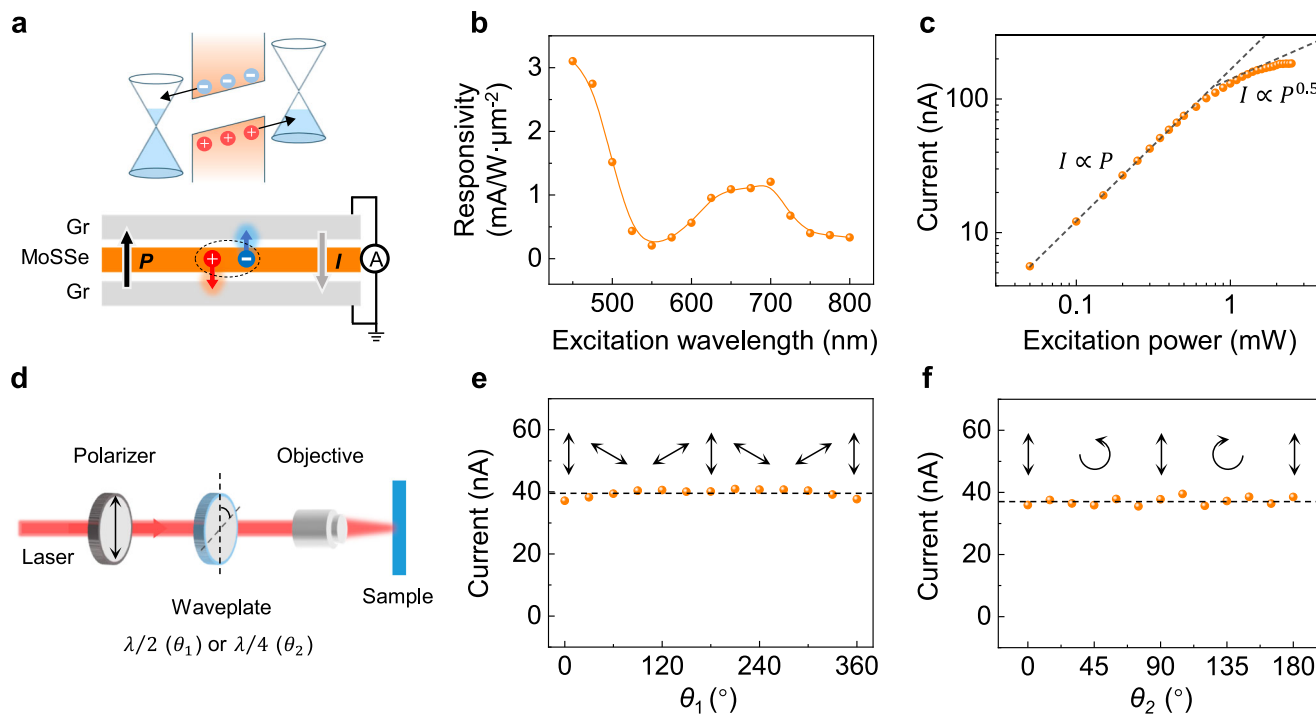


Fig. 4 | Depolarization field-dominated photocurrent generation in the MoSSe devices. **a** Schematic of the band alignment (top) and the photocarrier transfer process (both electrons and holes) in the device (bottom). The intrinsic polarization (black arrow) in the MoSSe layer induces charges in the graphene electrodes that do not fully compensate for the polarization charges. The existing depolarization field drives the photocarriers to the interface and leads to a photocurrent (gray arrow) in the direction opposite to the polarization direction. **b** Excitation wavelength-dependent photocurrent responsivity. This peak corresponds to the exciton resonance of MoSSe. The dots are the experimental data and the solid line

is used for eye guidance. **c** Excitation power-dependent spontaneous photocurrent. In order to characterize the slope clearly, logarithmic coordinates are used in the figure representation. The dots are the experimental data and the dashed lines correspond to the linear and square-root fit, respectively. **d** Schematic of the polarization-dependent photocurrent measurement. The polarization of the incident light can be tuned by combining a linear polarizer with a $\lambda/2$ waveplate or a $\lambda/4$ waveplate. Linear polarization direction (**e**) and circular ellipticity (**f**) dependence of the photocurrent by varying the angle of the $\lambda/2$ or $\lambda/4$ waveplates, θ_1 or θ_2 , respectively. The horizontal dashed lines are used for eye guidance.

integrated, and flexible thin-film optoelectronic and photovoltaic devices.

In conclusion, by atomic substitutional engineering of the surfaces of 2D TMDs for symmetry breaking, giant APE arises in a Janus structure with an asymmetric atomic lattice and an intrinsic out-of-plane polarization. Unlike conventional photovoltaics, the enhanced depolarization field-induced photocurrent provides an alternative mechanism for developing photovoltaic devices and photodetectors based on thin 2D layered polar materials. Combined with the ultrafast photoresponse time, potential applications in future optical microsensing, micro-actuation, and high-speed optical detection will be developed for next-generation compact and flexible optoelectronic devices.

Methods

Sample preparation and device fabrication

The Janus MoSSe structure was prepared by the postprocess of as-produced MoS₂ film on an a-plane sapphire substrate. The as-grown MoS₂ and the ZnSe crystal plate were placed in a face-to-face manner using two pieces of mica. The Se substitution was performed at 870 °C and the system pressure was kept at -1 torr with 120 sccm Ar and 5 sccm H₂. This postprocess time was kept for 30 minutes and the system was naturally cooled down to room temperature after substitution. The devices were fabricated by using the dry transfer method under a microscope. BN and graphene flakes were mechanically exfoliated onto the SiO₂/Si substrates and transferred using poly(propylene) carbonate (PPC). Janus MoSSe films were extracted from the substrates and transferred using poly(methyl methacrylate) (PMMA). The Au electrodes were transferred onto the device using PPC.

Device Characterization

Optical images were taken with an Olympus BX51M microscope. Raman and PL spectra were measured by the WITec alpha300R system with a laser excitation wavelength of 514 nm. The cross-sectional transmission electron microscopy samples were prepared using the focused ion beam technique (Thermo Fisher Helios G4 UX). The atomically-resolved STEM experiments were performed in an FEI Titan Themis G2 300 operated at 300 kV. The X-ray photoelectron spectroscopy (XPS) measurements were performed using an ESCALAB 250X system (Thermo Fisher Scientific) and excited by monochromatic Al K α radiation.

Incident angle-dependent SHG measurement

The SHG was excited by femtosecond pulses from a Coherent laser (-150 fs, 250 kHz) generated by a Ti:sapphire oscillator. A collimated p-polarized pulse laser beam (with a 2 mm spot size) was guided into the back aperture of a Nikon objective (50x, NA = 0.8). The incident angle was tuned by moving the beam position at the objective's back aperture using a retroreflector on a translational stage. The excitation wavelength was 800 nm, and the SHG signal was collected using the same objective after filtering the excitation laser, and analyzed by a polarizer along p polarization to exclude s polarized SHG induced by the in-plane dipole. In order to extinct the in-plane SHG component along p polarization, the sample was rotated to a specific crystal angle. The experiment setup is shown in Supplementary Fig. S3.

Time-resolved photocurrent measurements

Two cross-polarized pulsed beams (minimize interference near zero delay, each with -100 fs pulse width and 710 nm wavelength, sourced

from a Ti:sapphire 80 MHz oscillator) were focused on Janus MoS₂ devices. The devices were operated without external bias for a spontaneous response assessment. Photocurrent modulation within the device was induced by one beam pulse chopped at 1300 Hz. This modulation was sensitive to the interaction with the second beam pulses, delayed through a motorized delay line by Δt , and then the photocurrent's dependency on the delay time was analyzed. The response time is the time constant τ determined through the exponential fitting.

Data availability

The Source Data underlying the figures of this study are available with the paper. All raw data generated during the current study are available from the corresponding authors upon request. Source data are provided with this paper.

References

- Vladimir, M. F. & Popov, B. N. Anomalous photovoltaic effect in ferroelectrics. *Sov. Phys. Usp.* **21**, 981 (1978).
- Martin, L. W. & Rappe, A. M. Thin-film ferroelectric materials and their applications. *Nat. Rev. Mater.* **2**, 16087 (2017).
- Brody, P. S. High voltage photovoltaic effect in barium titanate and lead titanate-lead zirconate ceramics. *J. Solid State Chem.* **12**, 193–200 (1975).
- Yang, S. Y. et al. Above-bandgap voltages from ferroelectric photovoltaic devices. *Nat. Nanotechnol.* **5**, 143–147 (2010).
- Nechache, R. et al. Bandgap tuning of multiferroic oxide solar cells. *Nat. Photon.* **9**, 61–67 (2015).
- Spanier, J. E. et al. Power conversion efficiency exceeding the Shockley-Queisser limit in a ferroelectric insulator. *Nat. Photon.* **10**, 611–616 (2016).
- Mehta, R. R., Silverman, B. D. & Jacobs, J. T. Depolarization fields in thin ferroelectric films. *J. Appl. Phys.* **44**, 3379–3385 (1973).
- Fridkin, V. M. Bulk photovoltaic effect in noncentrosymmetric crystals. *Crystallogr. Rep.* **46**, 654–658 (2001).
- Yang, M.-M., Kim, D. J. & Alexe, M. Flexo-photovoltaic effect. *Science* **360**, 904–907 (2018).
- Li, Y. et al. Enhanced bulk photovoltaic effect in two-dimensional ferroelectric CuInP₂S₆. *Nat. Commun.* **12**, 5896 (2021).
- Starkiewicz, J., Sosnowski, L. & Simpson, O. Photovoltaic effects exhibited in high-resistance semi-conducting films. *Nature* **158**, 28–28 (1946).
- Goldstein, B. & Pensak, L. High-voltage photovoltaic effect. *J. Appl. Phys.* **30**, 155–161 (1959).
- Koch, W. T. H., Munser, R., Ruppel, W. & Würfel, P. Bulk photovoltaic effect in BaTiO₃. *Solid State Commun.* **17**, 847–850 (1975).
- Levi Aharoni, H., Azulay, D., Millo, O. & Balberg, I. Anomalous photovoltaic effect in nanocrystalline Si/SiO₂ composites. *Appl. Phys. Lett.* **92**, 112109 (2008).
- Chen, G. et al. Evidence of a gate-tunable Mott insulator in a trilayer graphene moiré superlattice. *Nat. Phys.* **15**, 237–241 (2019).
- Zhang, Y. J. et al. Enhanced intrinsic photovoltaic effect in tungsten disulfide nanotubes. *Nature* **570**, 349–353 (2019).
- Zhang, X. X. et al. Gate-tunable spin waves in antiferromagnetic atomic bilayers. *Nat. Mater.* **19**, 838–842 (2020).
- Shi, Y. et al. Electronic phase separation in multilayer rhombohedral graphite. *Nature* **584**, 210–214 (2020).
- Zhou, H., Xie, T., Taniguchi, T., Watanabe, K. & Young, A. F. Superconductivity in rhombohedral trilayer graphene. *Nature* **598**, 434–438 (2021).
- Akamatsu, T. et al. A van der Waals interface that creates in-plane polarization and a spontaneous photovoltaic effect. *Science* **372**, 68–72 (2021).
- Du, L. J. et al. Engineering symmetry breaking in 2D layered materials. *Nat. Rev. Phys.* **3**, 193–206 (2021).
- Xu, H. et al. Colossal switchable photocurrents in topological Janus transition metal dichalcogenides. *NPJ Comput. Mater.* **7**, 31 (2021).
- Stern, M. V. et al. Interfacial ferroelectricity by van der Waals sliding. *Science* **372**, 1462–1466 (2021).
- Yasuda, K., Wang, X. R., Watanabe, K., Taniguchi, T. & Jarillo-Herrero, P. Stacking-engineered ferroelectricity in bilayer boron nitride. *Science* **372**, 1458–1462 (2021).
- Yang, D. et al. Spontaneous-polarization-induced photovoltaic effect in rhombohedrally stacked MoS₂. *Nat. Photon.* **16**, 469–474 (2022).
- Wu, J. D. et al. Ultrafast response of spontaneous photovoltaic effect in 3R-MoS₂-based heterostructures. *Sci. Adv.* **8**, eade3759 (2022).
- Rogée, L. et al. Ferroelectricity in untwisted heterobilayers of transition metal dichalcogenides. *Science* **376**, 973–978 (2022).
- Wang, X. R. et al. Interfacial ferroelectricity in rhombohedral-stacked bilayer transition metal dichalcogenides. *Nat. Nanotechnol.* **17**, 367–371 (2022).
- Liang, J. et al. Shear strain-induced two-dimensional slip avalanches in rhombohedral MoS₂. *Nano Lett.* **23**, 7228–7235 (2023).
- Dong, Y. et al. Giant bulk piezophotovoltaic effect in 3R-MoS₂. *Nat. Nanotechnol.* **18**, 36–41 (2023).
- Lu, Z. et al. Fractional quantum anomalous Hall effect in multilayer graphene. *Nature* **626**, 759–764 (2024).
- Lu, A. Y. et al. Janus monolayers of transition metal dichalcogenides. *Nat. Nanotechnol.* **12**, 744–749 (2017).
- Zhang, J. et al. Janus monolayer transition-metal dichalcogenides. *ACS Nano* **11**, 8192–8198 (2017).
- Trivedi, D. B. et al. Room-temperature synthesis of 2D Janus crystals and their heterostructures. *Adv. Mater.* **32**, 2006320 (2020).
- Guo, Y. et al. Designing artificial two-dimensional landscapes via atomic-layer substitution. *Proc. Natl. Acad. Sci.* **118**, e2106124118 (2021).
- Dong, L., Lou, J. & Shenoy, V. B. Large in-plane and vertical piezoelectricity in Janus transition metal dichalcogenides. *ACS Nano* **11**, 8242–8248 (2017).
- Tang, X. & Kou, L. Z. 2D Janus transition metal dichalcogenides: properties and applications. *Phys. Status Solidi B* **259**, 2100562 (2022).
- Shi, J. et al. Giant room-temperature nonlinearities in a monolayer Janus topological semiconductor. *Nat. Commun.* **14**, 4953 (2023).
- Sun, D. et al. Ultrafast hot-carrier-dominated photocurrent in graphene. *Nat. Nanotechnol.* **7**, 114–118 (2012).
- Massicotte, M. et al. Picosecond photoresponse in van der Waals heterostructures. *Nat. Nanotechnol.* **11**, 42–46 (2016).
- Tan, L. Z. et al. Shift current bulk photovoltaic effect in polar materials—hybrid and oxide perovskites and beyond. *NPJ Comput. Mater.* **2**, 16026 (2016).
- Dai, Z. & Rappe, A. M. Recent progress in the theory of bulk photovoltaic effect. *Chem. Phys. Rev.* **4**, 011303 (2023).
- Lopez-Varo, P. et al. Physical aspects of ferroelectric semiconductors for photovoltaic solar energy conversion. *Phys. Rep.* **653**, 1–40 (2016).

Acknowledgements

This work was supported by the National Key R&D Program of China (2023YFB3208102 (C.L.), 2021YFA1400201 (H.H.) and 2022YFA1403504 (K.L.)), National Natural Science Foundation of China (52025023 (K.L.), 51991342 (K.L.), 12422406 (H.H.), 12374167 (H.H.), 12304204 (C.L.), 52302189 (L.D.)), Guangdong Major Project of Basic and Applied Basic Research (2021B0301030002 (E.W. and K.L.)), the Strategic Priority Research Program of Chinese Academy of Sciences (XDB33000000 (K.L.)), China Postdoctoral Science Foundation (2022M710232 (C.L.)), and the New Cornerstone Science Foundation through the XPLOER PRIZE (K.L.).

Author contributions

K.L., H.H. and E.W. supervised and conceived the projects. C.L., T.L. and L.D. fabricated the devices and performed the photocurrent experiments. X.S., G.X. and M.Z. synthesized the samples. C.L. and X.S. performed the PL, Raman, SHG and XPS characterizations. Q.G. conducted the STEM experiments. C.H., Y.Y. and G.Y. helped to illustrate the mechanisms. J.Y. and Z.S. contributed to the interpretation of the results. All the authors discussed and contributed to writing the paper.

Competing interests

The authors declare no competing interests.

Additional information

Supplementary information The online version contains supplementary material available at <https://doi.org/10.1038/s41467-024-55623-x>.

Correspondence and requests for materials should be addressed to Hao Hong, Enge Wang or Kaihui Liu.

Peer review information *Nature Communications* thanks Chao Ma and the other, anonymous, reviewers for their contribution to the peer review of this work. A peer review file is available.

Reprints and permissions information is available at <http://www.nature.com/reprints>

Publisher's note Springer Nature remains neutral with regard to jurisdictional claims in published maps and institutional affiliations.

Open Access This article is licensed under a Creative Commons Attribution-NonCommercial-NoDerivatives 4.0 International License, which permits any non-commercial use, sharing, distribution and reproduction in any medium or format, as long as you give appropriate credit to the original author(s) and the source, provide a link to the Creative Commons licence, and indicate if you modified the licensed material. You do not have permission under this licence to share adapted material derived from this article or parts of it. The images or other third party material in this article are included in the article's Creative Commons licence, unless indicated otherwise in a credit line to the material. If material is not included in the article's Creative Commons licence and your intended use is not permitted by statutory regulation or exceeds the permitted use, you will need to obtain permission directly from the copyright holder. To view a copy of this licence, visit <http://creativecommons.org/licenses/by-nc-nd/4.0/>.

© The Author(s) 2025